STUDY OF ENDOSCOPY FOR DENTAL TREATMENT

Shinji Yoshii[1], Yupeng Zhang[3], Satoshi Ikezawa[3], Chiaki Kitamura[1], Tatsuji Nishihara[2], Toshitsugu Ueda[3]

1. Division of Pulp Biology, Operative Dentistry, and Endodontics,
2. Division of Infections and Molecular Biology Kyushu Dental College
2-6-1, Manazuru, Kokurakita, Kitakyushu, Fukuoka 803-8580, Japan
3. Graduate School of Information, Production and Systems, Waseda University
2-7 Hibikino,Wakamatsu-ku, Kitakyushu-shi, Fukuoka 808-0135, Japan

r08yoshii@fa.kyu-dent.ac.jp

Submitted: Jan. 5, 2013 ***Accepted: Jan. 31, 2013*** ***Published: Feb. 20, 2013***

Abstract*—Observation of the oral cavity microstructure is an important factor for a successful dental treatment. None of the many currently available diagnostic equipment can accurately observe the microstructure. In this study, we have designed an endoscope with a single graded-index multimode fiber of 600-μm diameter that can reach the narrow spaces in the oral cavity and can perform both image acquisition and sample illumination using a prism beam splitter, unlike the conventional endoscope using separate fibers. Thus, the side branch of the teeth and the subgingival calculus can be accurately observed with a resolution of up to 10 μm.

Keywords*—dental therapy, root canal, graded-index image fiber

I. INTRODUCTION

In dental practice, accurate diagnosis and delicate treatment of the defects in the narrow root canals of the oral cavity are required. Root canal therapy is particularly one of the complicated dental treatments because of the difficulty in direct observation. It is a surgical procedure used when the tooth decay has progressed to the dental pulp including the nerves. First, the dental caries should be removed and the root canal accommodating the dental pulp should be exposed. Second, the dental pulp is removed by using a file and a reamer. However, the root canals exhibit a complicated morphology [1], [2]. The root canals comprise a group of complicated structures called collaterals, which branch near the apex. The diagnosis of the collaterals by observing from the orifice of the root canals is very difficult. The pain induced by the removal of the remnants of the dental pulp cannot be reduced; instead, it increases. As a result, it is currently impossible to clearly perform a chairside observation of the collaterals of the root canals in real time. The mandibular molars are shown in Figure1.

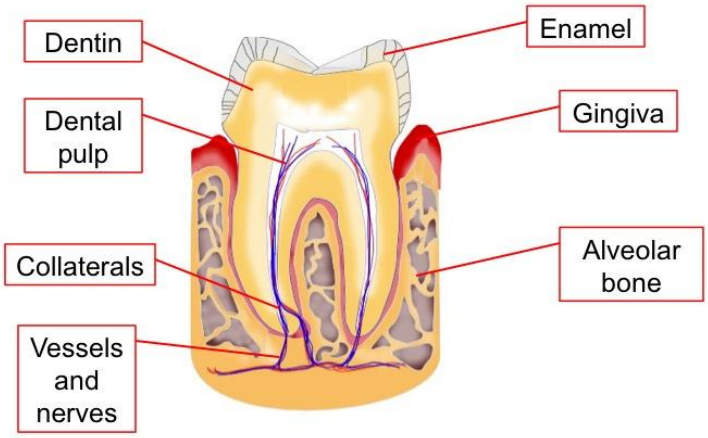

Figure 1. Cross-section of human mandibular molars

Human tooth is mainly composed of three layers of hard tissue: the cementum, dentin, and enamel, as well as the pulp. The nerves and blood vessels in the pulp are located inside the root canal, from the exterior to the interior of the tooth, which are additionally involved in the sensation of the tooth. The teeth are surrounded by the gingival, alveolar bone, and periodontal ligament. The tooth structure is not simple, and the root canal exhibits different aspects, which branches inside the tooth. Currently, many dental treatments rely on the experience and intuition of the dentists because it is impossible to directly observe the lesions inside the dark

and narrow root canals. However, the diagnostic accuracy has currently been improved by using a microscope or cone-beam Computed Tomography (CBCT) as shown by Figures 2 and 3 [3-17].

Figure 2. Picture of microscope used for dental treatment

Figure 3. Picture of CBCT device

A microscope can diagnose the microcracks in the tooth and abnormalities such as microdamage and can provide a magnification of up to 20 times for the restoration from outside the oral cavity in the real time. Thus, it is possible to perform a more accurate treatment. However, if the root canal is curved, we cannot observe the root apex. A CBCT with a voxel size of up to 80 μm can be used for the observation of the tooth interior, and it enables

a noninvasive diagnosis. However, it cannot perform real-time observation because of some exposure issues. In this study, our objective is to develop a novel diagnostic device with a high resolution to observe the fine structures inside the tooth, particularly, the periapical tissues and periodontal pockets. It is inexpensive and comprises a simple design. We use an image fiber with a diameter of 600 μm, 15000 pixels, and resolution of approximately 6 μm. We design the device in such a manner that it enables to both obtain a clear image and illuminate the sample with light using a graded-index (GRIN) fiber. As a result, we can obtain an image of the tooth interior, even though it is narrow and dark. We use a GRIN fiber (FIGH-15-480S, 15000 pixels, diameter of 600 μm) that is inserted in a CMOS sensor, an objective lens, a prism beam splitter (PBS), and an optical fiber, all arranged in a straight line. At the PBS, we arrange the optical fiber at right angle, and the PBS is illuminated. Half the amount of light incident on the PBS is reflected toward the GRIN fiber and illuminates the sample through the fiber. Oil stagnates between the PBS and the image fiber because of the reflection at the interface. The tip of the fiber contacts the sample. Further, we suppress the reflection and scattering of light in the system by placing a mask of 2.5 mm at the center of the light source lens and eliminate the halation that appears on the image by image processing. It is possible to simultaneously obtain a clear image and illuminate the sample with light through the image fiber with this device. The quality of this image is almost same as that of the image obtained with an external illumination. The resolution is approximately 10 μm. This value is sufficient to diagnose the cracks and collaterals of the root canals. These results suggest that this device has the potential for obtaining vivid images of the fine structures in the root canal.

II. MATERIAL AND METHODS

The system schematic is shown in Figure 3.

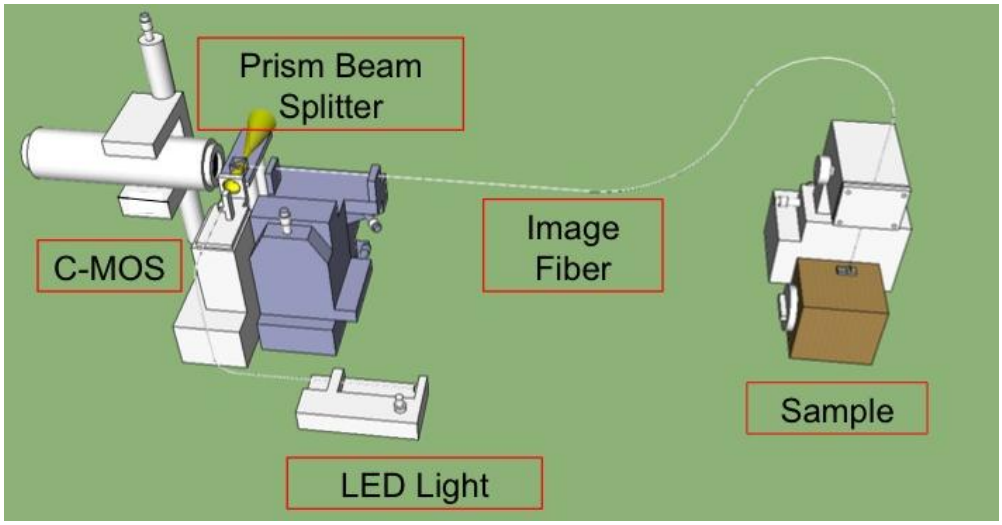

Figure 3. System schematic

This system consists of a microscope with a CMOS image sensor, a PBS, an optical fiber connected to an LED as the light source, a double-convex spherical lens to converge the light beams emanating from the optical fiber, and a GRIN image fiber.

The GRIN image fiber is fabricated by Fujikura Corp. It consists of 15000 parallel cores (pixels) located within the same silica jacket. The fiber diameter and image circle diameter are 480 μm and 450 μm, respectively, and the outer coating diameter is approximately 570 μm. The minimum bending radius is 50 mm. The cross-section of the fiber is illustrated in Figure 4.

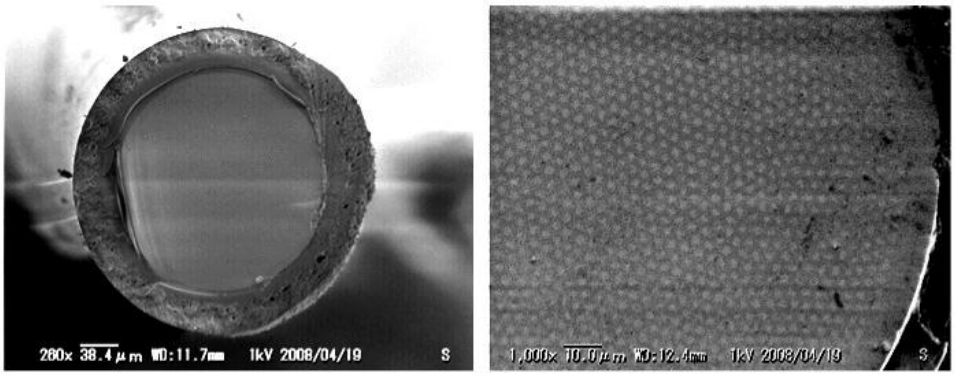

Figure 4. Cross-section of GRIN image fiber (SEM images)

The material of the fiber core is GeO_2-SiO_2, and the clad is composed of F-SiO_2. The fiber is coated with a silicone resin. The fiber with this diameter is small enough to be inserted into the root canal of the tooth for lesion observation. As shown in Figure 5, the apex of the root canal

is approximately 100 μm in diameter, which is the narrowest part. The diameter increases from the apex to the upper part of the root canal, forming a conical shape. The widest area is not less than 1 mm in diameter.

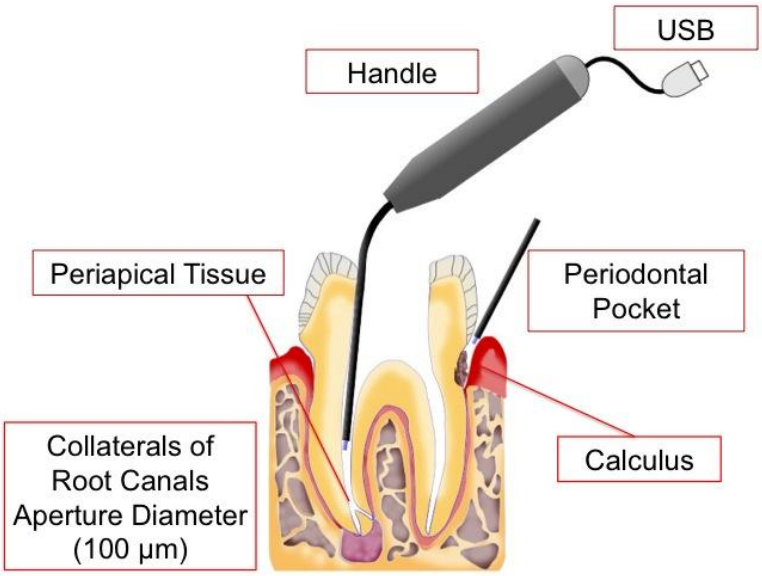

Figure 5. Cross-section of root canals and its observation using our diagnostic device; diameter of apex and collaterals of root canals is 100 μm.

We have employed an LED light source in our system, which has been widely used in a variety of medical equipment including the dental diagnostic and treatment devices. The illumination by the LED light source is harmless to the human body and very effective [18-21]. Table 1 lists the LED specifications, and Figure 6 shows the relationship between the measured wavelength and intensity of the LED. This figure shows a peak at 450 nm.

Table 1: Specifications of LED

Type	Size	Deg	Color	Lens	Voltage	Intensity
OSW4XME3C1S	19.9 mm	120	Pure white	Yellow diffused	3.3 V	200 lm

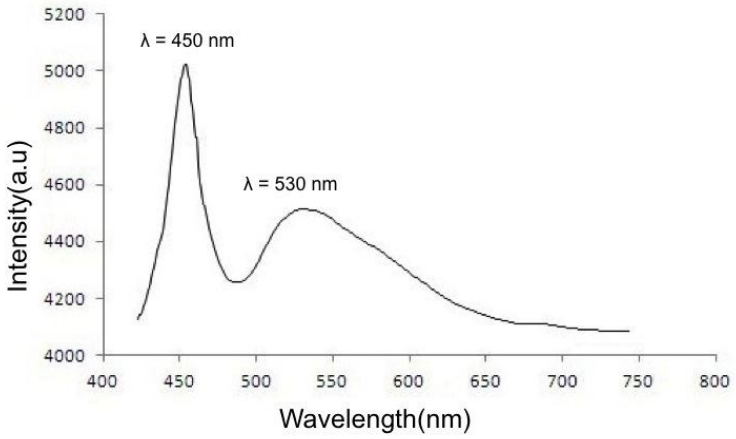

Figure 6. Relationship between wavelength and intensity of LED

As shown in Figure 7, the LED light source is connected to one end of the optical fiber. The light intensity of the LED source can be adjusted by using a pulse width modulation (PWM) circuit as shown in Figure 8.

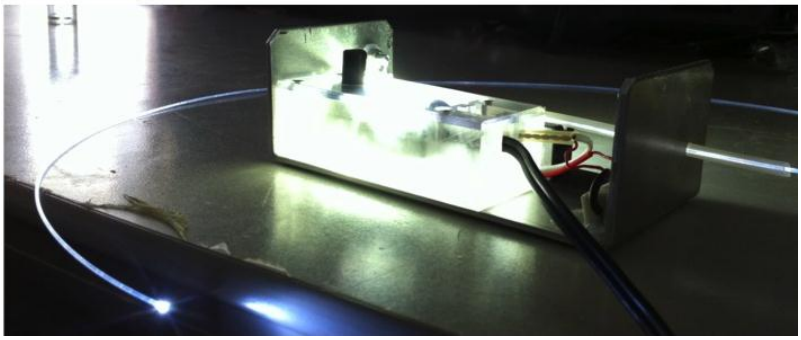

Figure 7. LED light source is connected to one end of optical fiber. Photograph of the LED light source when the light is turned on. The light emanating from the LED enters one end of the fiber and is output from the other end.

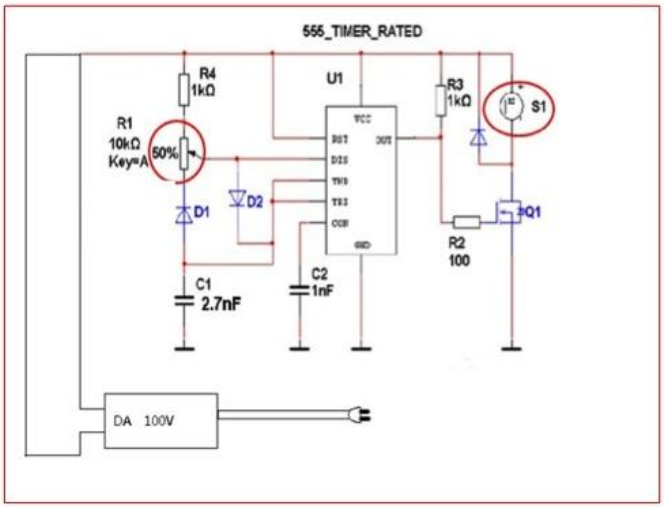

Figure 8. Circuit of light source. The light intensity of the LED source can be adjusted by using a pulse width modulation (PWM) circuit.

As shown in Figure 9, when we place a mask at the center of the condensing lens, a ring-shaped light emanates and the reflected light is not transferred to the surface of the image-obtaining plane of the objective lens, which is irradiated with the ring-shaped light. Figure 10 shows the relationship between the image-obtaining plane of the objective lens and the mask on the condensing lens, which is expressed in equations (1) and (2), and Figure 11 shows the relationship between the intensity of the reflected light and the light-shielding mask diameter. d_A is the aperture size, d'_M is the diameter of the shadow formed by the mask, d_M is the mask diameter, and E_V is the amount of light flux per unit area of the reflected light.

$$I \propto \frac{1}{4}\left(\pi {d_A}^2 - \pi {d'_M}^2\right) \times E_V \quad (1)$$

$$d'_M \propto d_M \quad (2)$$

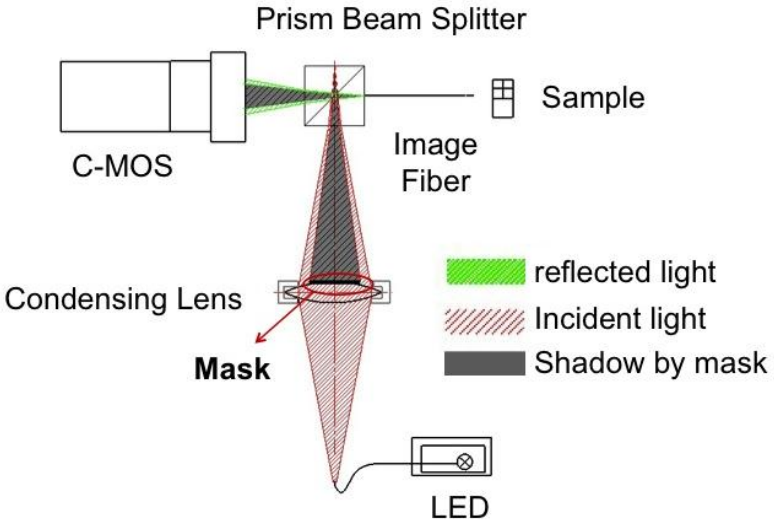

Figure 9. Conceptual schematic of the shadow mask. We purpose to reduce the center of light to reflections by masking the condensing lens

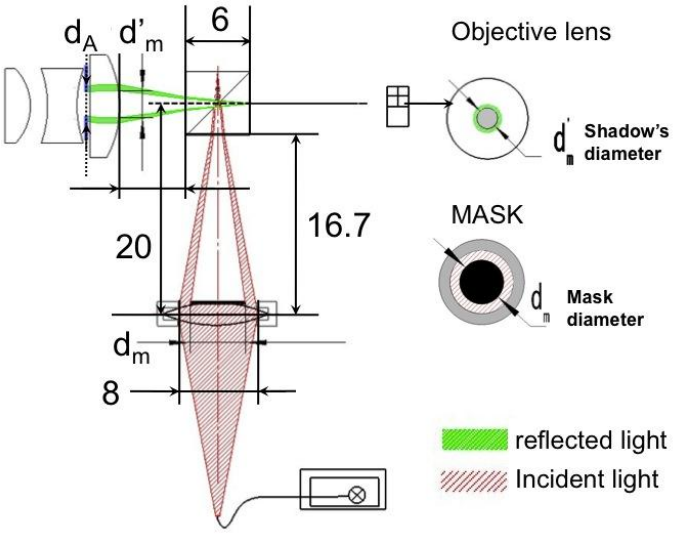

Figure 10. Relationship between mask and shadow of objective lens surface. We calculate the diameter of the ideal mask on the basis of this relationship. The ideal mask diameter is 2.424 mm.

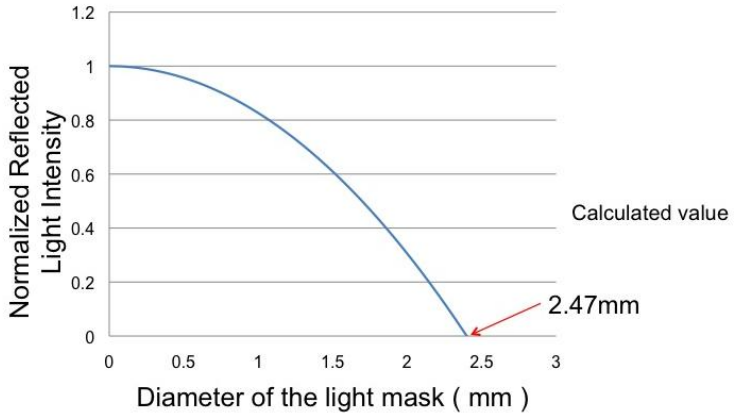

Figure 11. Relationship between intensity of reflected light and light-shielding mask diameter

The light is not reflected on the PBS surface by using a mask of 2.4 mm. At this point, the irradiation light intensity is 90.4%, as shown in Figure 12.

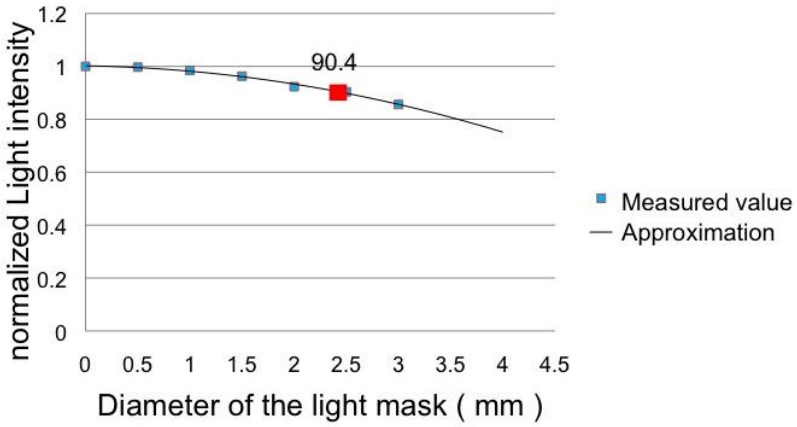

Figure 12. Relationship between intensity of irradiation light and light-shielding mask diameter. Irradiation light intensity is 90.4%.

We have employed a polarized PBS in our diagnostic system. The light reaching the PBS surface is orthogonally polarized. The s-polarized beam (whose polarization is perpendicular to the plane of incidence) is reflected on the GRIN image fiber and the p-polarized beam (whose polarization is in the plane of incidence) passes through the fiber. The light transmitted from

the image fiber further illuminates the sample patterns to be observed. Glycerin is filled between the PBS and one tip of the image fiber and between the other tip of the image fiber and the sample in order to suppress the reflection at their surfaces. The sample patterns are fabricated using the focused ion beam (FIB) technique. Four line and space widths are fabricated on the surface of the sample, namely, 10 μm, 20 μm, 50 μm, and 100 μm, which are shown in Figure13. A clear image of the sample patterns can be obtained by direct contact of the sample surface with the GRIN image fiber tip. The CMOS microscope used in our system performs real-time image observation and capture. Its design is quite simple, and it is available at a very low price. It consists of only two objective lenses, which are separated at a fixed distance. The magnification can be adjusted from 10X to 1000X. A USB cable is connected to a computer, and the observed image is displayed on the computer screen in real time.

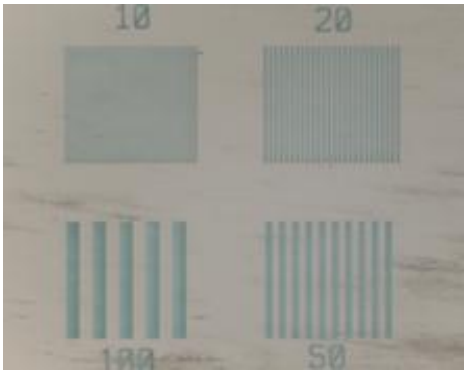

Figure 13. Sample patterns with four different line and space widths: 10 μm (top left), 20 μm (top right), 50 μm (lower right) and 100 μm (lower left)

The aforementioned reflection on the PBS surface manifests as a halation around the center and four corners of the observed sample image. In addition to filling up with glycerin and using light-shielding mask on the double convex lens surface, the halation can be further suppressed by image processing. This is realized by image subtraction between the two captured images: one image is captured without the GRIN image fiber and sample patterns such that the captured image only includes the halation due to the reflection on the PBS surface (see Figure15 (b) in Section III). The other one is the captured image of the sample pattern using the GRIN image fiber (see, Figure15 (a) in Section III).

III. RESULTS AND DISCUSSION

In this section, we investigate the performance of the diagnostic system by real-time observation and capture of the images of the sample patterns. The fabricated sample patterns are shown in Figure 12. The numbers on the patterns indicate the different line and space widths in micrometer. The GRIN image fiber tip directly contacts the sample surface during observation. Our objective is to observe the patterns without the help of an external illumination on the sample surface. The sample is illuminated simply by the GRIN image fiber, where the light is transmitted from the LED source (we call it internal illumination). Further, the images of the patterns are transmitted back to the other side of the image fiber and finally reach the CMOS image sensor of the microscope. For evaluating the captured image quality under the condition of internal illumination, we compare the image obtaining using an internal illumination with that obtained using an external light source for illuminating the surface of the sample. Figure 14 shows the real-time observed and captured images of the four different patterns: 10 μm, 20 μm, 50 μm, and 100 μm line, as well as space. The upper four images shown in Figure 14 were captured when a halogen lamp externally irradiated the surface of the sample. The lower four images were captured using an internal illumination. It can be directly observed from Figure 14 that the contrast of the captured image using an internal illumination equals to that using an external illumination, except that the halation around the center and corners of the lower four images slightly reduces the contrast. In addition, several blots can be observed in Figures 14 (f) and (h) owing to direct contact of the sample surface with the image fiber. We have quantified the contrast by the following equations:

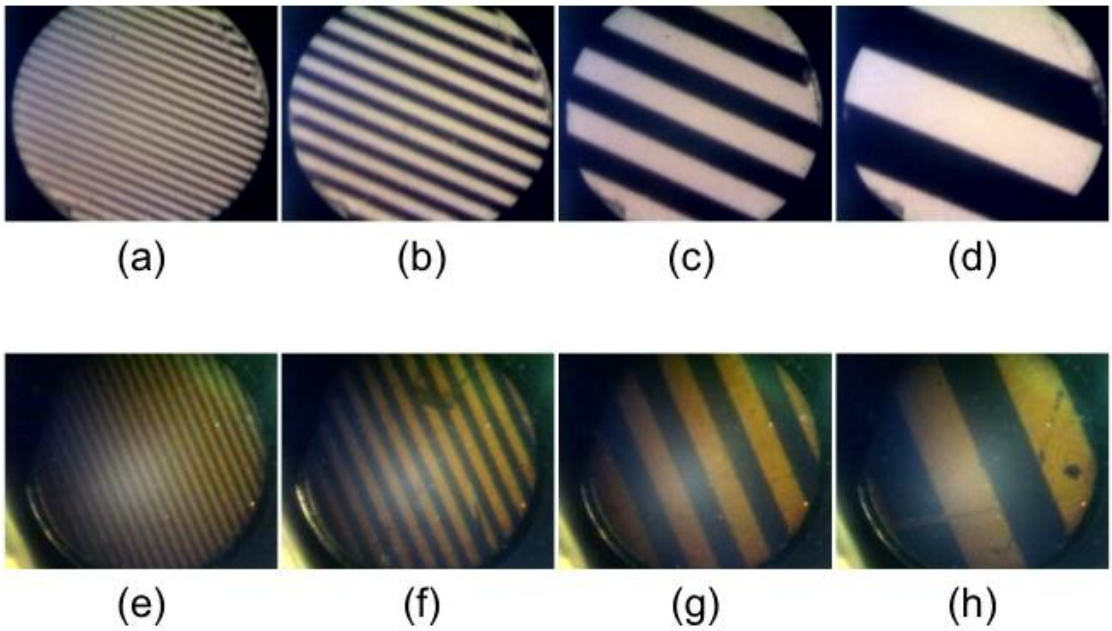

Figure 14. Captured images of four sample patterns using external and internal illuminations. (a), (b), (c), and (d) are captured images of 10-μm, 20-μm, 50-μm, and 100-μm line and space widths using external illumination. (e), (f), (g), and (h) are captured images of 10-μm, 20-μm, 50-μm, and 100-μm line and space widths using internal illumination.

$$Ci = \frac{I_{\max} - I_{\min}}{I_{\max} + I_{\min}} \qquad (3)$$

$$C = \left(\sum_{i=1}^{n} Ci \right) / n \qquad (4)$$

where C*i* is the contrast value of the *i*th region of the captured image and C is the overall contrast of the entire image, which is obtained by arithmetic mean of the contrasts of *n* different regions. $I_{\max}$ and $I_{\min}$ denote the maximum and minimum intensities in the *i*th region, respectively. The higher the value of C, the easier it is to distinguish a line from a space. We have computed the contrast values for 10-μm and 20-μm line and space widths using external and internal illuminations. Five regions are selected for contrast computation: upper left, upper right, lower left, lower right, and central regions. We have neglected the image boundaries and pixel vacancies, which result in incorrect contrast values. The results are summarized in Table 2.

Table 2: Contrast comparison for 10-μm and 20-μm line and space widths using external and internal illuminations.

Line and Space Width	External	Internal
10 μm	0.4362	0.5669
20 μm	0.6824	0.5944

The results summarized in Table 2 demonstrate that the contrast difference between the external and the internal illumination is smaller than 0.13 in the case of 10-μm and 20-μm line and space widths, which suggests that the captured images using an internal illumination have an image contrast similar to that of the images using an external illumination. However, the halation is visible around the center and corners of the captured image in the case of internal illumination because of the reflection on the PBS surface and fiber tips. We have used an image subtraction algorithm described in Section II B to further suppress the halation. The results are shown in Figure 15. Figure 15 (a) shows the captured image of the sample pattern using the GRIN image fiber. The halation is clearly visible around the center and corners of the image. Figure 15 (b) shows the captured image without the GRIN image fiber and sample patterns, which includes only the halation. By subtracting (b) from (a), we obtain (c), in which the halation is suppressed.

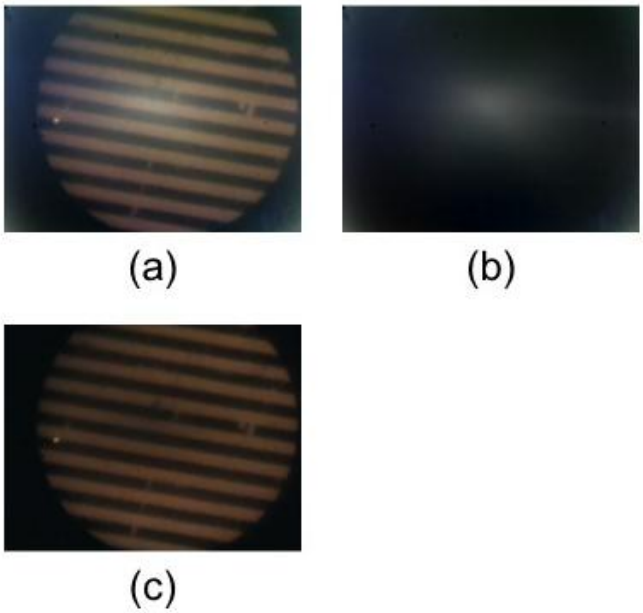

Figure 15. Halation suppression by image subtraction. (a) Captured image of the sample pattern of 20-μm line and space width using the GRIN image fiber (b) Captured image without the GRIN image fiber and sample. (c) Resultant image without halation.

Thus far, we have shown that the sample patterns up to 10-μm line and space widths can be clearly observed using a single image fiber for both illumination and image transmission. However, the real-time dental diagnosis and treatment require an optical system with a higher capability to distinguish the lesions from the normal tissues. The next stage of our research is to improve the captured image quality and observe the in vivo fine tissues inside the root canals of the human teeth. In addition, the current system using an internal illumination cannot observe an object if the distance between the GRIN image fiber and the object is not zero. The object distance can be increases by attaching a GRIN lens to the image fiber tip. Our image fiber is capable of observing the tissues near the fiber by directly contacting the tissues; however, it cannot reach the apex of the root canals where the diameter is approximately 100 μm because the fiber's outer diameter is 570 μm. Therefore, an increase in the distance between the object and the image fiber is necessary in order to observe the deep tissues.

IV. CONCLUSION

In this paper, we have proposed a low-cost dental diagnostic system that can carry out real-time observation of the interior of the narrow root canals of the tooth. This system uses a single GRIN image fiber for both sample illumination and image transmission, and it successfully captures the images of the sample patterns of up to 10-μm line and space widths with an acceptable contrast. Our system has the advantage of simultaneously illuminating and obtaining a clear image of the observed tissue through a single image fiber, and the probe diameter of this endoscope is small enough to be fitted into the root canals of the oral cavity for observation. The current system can only observe an object when the object distance from the image fiber is zero. An increase in the object distance, which can be realized by attaching a GRIN lens to the tip of the image fiber on one side of the sample, will be dealt with in our future work.

V. ACKNOWLEGMENT

The author would like to thank Prof. Zimin and Mr. Tsuno and Mr. Chen for their support and direction for this project.

REFERENCES

[1] F.J. Vertucci, “Root canal anatomy of the human permanent teeth,” Oral Surg Oral Med Oral Pathol., vol. 58, pp. 589-599, 1984.

[2] F.J. Vertucci, “Root canal morphology and its relationship to endodontic procedures,” Endodontic Topics, vol. 10, pp. 3-29, 2005.

[3] J.K. Bahcall and J.T. Barss, “Fiberoptic endoscope usage for intracanal visualization,” J Endod., vol. 27, pp. 128-129, 2001.

[4] J.K. Bahcall and J. Barss, “Orascopic visualization technique for conventional and surgical endodontics,” Int Endod J., vol. 36, pp. 441-447, 2003.

[5] P. Mozzo, C. Procacci, A. Tacconi, P. Tinazzi Martini, and I.A. Bergamo Andreis, “A new volumetric CT machine for dental imaging based on the cone-beam technique: preliminary results,” Euro Radiol., vol. 8, pp. 1558-1564, 1998

[6] A. Dawood, S. Patel, and J. Brown, “Cone beam CT in dental practice,” Br Dent J. vol. 207, no. 1, pp. 23-8, 2009.

[7] M.D. Fabbro and S. Taschieri, “Endodontic therapy using magnification devices: a systematic review,” J Dent., vol. 38, no. 4, pp. 269-75. 2010.

[8] M.K. Nair and U.P. Nair, “Digital and advanced imaging in endodontics: a review,” J Endod., vol. 3, pp. 1-6, 2007.

[9] B.W. Small, “Cone beam computed tomography,” Gen Dent., vol. 55, pp. 179-181, 2007.

[10] R.P. Matherne, C. Angelopoulos, J.C. Kulild, and D. Tira, “Use of cone-beam computed tomography to identify root canal systems in vitro,” J Endod., vol. 34, pp. 87-89, 2008.

[11] T.P. Cotton, T.M. Geisler, D.T. Holden, S.A. Schwartz, and W.G. Schindler, “Endodontic applications of cone-beam volumetric tomography,” J Endod., vol. 33, pp. 1121-1132, 2007.

[12] S. Patel, A. Dawood, T.P. Ford, and E. Whaites, “The potential applications of cone beam computed tomography in the management of endodontic problems,” Int Endod J., vol. 40, pp. 818-830, 2007.

[13] T. Tsurumachi and K. Honda, “A new cone beam computerized tomography system for use in endodotic surgery,” Int Endod J., vol. 40, pp. 224-232, 2007.

[14] A.K. Suomalainen, A. Salo, S. Robinson, and J.S. Peltola, "The 3DX multi-image micro-CT device in clinical dental practice," Dentomaxillofac Radiol., vol. 36, pp. 80-85, 2007.

[15] M. Naitoh, S. Yamada, T. Noguchi, E. Ariji, J. Nagao, K. Mori, T. Kitasaka, and Y. Suenaga, "Three-dimensional display with quantitative analysis in alveolar bone resorption using cone-beam computerized tomography for dental use: a preliminary study," Int J Periodontics Restorative Dent., vol. 26, pp. 607-612, 2006.

[16] H. Tachibana and K. Matsumoto. "Application of X-ray computerized tomography in endodontics," Endod Dent Traumatol., vol. 6, pp. 16-20, 1990.

[17] K. Nakata, M. Naitoh, M. Izumi, K. Inamoto, E. Ariji, and H. Nakamura H, "Effectiveness of dental computed tomography in diagnostic imaging of periradicular lesion of each root of a multirooted tooth: a case report" J Endod., vol. 32, pp. 583-587, 2006.

[18] L. Zhang and K. Alemzadeh, "A 3-dimensional vision system for dental applications" Conf Proc IEEE Eng Med Biol Soc. 2007, pp. 3369-72, 2007.

[19] Ana K.S. Braz, Bernardo B.C. Kyotoku, Rodivan Braz, and Anderson S.L. Gomes, "Evaluation of crack propagation in dental composites by opticalcoherencetomography," Dent Mater., pp. 74-79, January 2009.

[20] K-C. Huang, C.-L. Chang, C.-H. Chang, and H.-C. Chang, "The pulse exciation of UV LED source for fluorescence detection," 2011 IEEE International Instrumentation and Measurement Technology Conference 1-4244-7933-9, 978-1-4244-7933-7.

[21] A.G. Mignani and F. Baldini, "In-vivo biomedical monitoring by fiber-optic systems," IEEE/OSA J Lightw Technol., vol. 13, no. 7, pp. 1396-1406, July 1995.